Plasmonic group IV transition metal carbide interfaces for solar-driven desalination

Matthew J. Margeson,[1] Mark Atwood,[1] and Mita Dasog[1]*

[1]*Department of Chemistry, Dalhousie University, Halifax, NS, Canada*

KEYWORDS. Plasmonics, photothermal, desalination, water evaporation, carbides

ABSTRACT

To combat the dwindling supply of freshwater, solar-driven desalination using plasmonic nanomaterials has emerged as a promising and renewable solution. Effective materials must exhibit high solar-to-vapor conversion efficiencies, be inexpensive, chemically stable, and maintain performance over time. Refractory plasmonic carbide nanomaterials are exciting candidates that could meet these demands but have not been as widely explored. Here, we investigate plasmonic carbide interfaces made of TiC, ZrC, and HfC nanoparticles loaded onto to a mixed cellulose ester (MCE) membrane gain insight into their solar-vapor generation and desalination potential. Evaporation rates and efficiencies were determined for tap water and saltwater with varying salt concentrations. Desalination using Atlantic Ocean water under 1 sun intensity yielded rates of 1.26 ± 0.01, 1.18 ± 0.02, and 1.40 ± 0.01 kg m^{-2} h^{-1}, with efficiencies of 86, 80, and 96% for TiC, ZrC, and HfC, respectively, under 1 sun illumination. Carbide interfaces effectively removed salt and metal ions from the water and were able to reject salt over extended periods of desalination and high salt concentrations of up to 35%. The effect of ambient temperature and relative humidity on the desalination process was also investigated which showed that the evaporation rates and efficiencies decrease with increasing humidity and decreasing room temperature. However, the performance of HfC was less affected by the changes in the ambient conditions compared to TiC and ZrC.

Introduction

Water scarcity is one of the most critical challenges facing modern society and it has been estimated that around two-thirds of the global population will face at least one month of water shortage annually by the year 2050.[1–3] Of these, 800 million people could be displaced by intense water scarcity within the next decade.[4] Factors such as increased consumption, geopolitical issues, pollution of water sources, among others play a role in further exacerbating this issue.[5] Therefore, increasing accessibility to water purification methods is crucial. Of the available technologies, desalination has been viewed as a promising way to address water shortages worldwide, owing to the relative availability of saltwater.[6] The majority of water desalination processes employ either thermal distillation techniques[7–9] or use reverse osmosis membranes[10–12] which permit water transport across a permeable membrane but reject salt ions. These techniques have inherent shortcomings such as a relatively low water flux to energy consumption ratio, durability, fouling, and selectivity issues, and intensive infrastructure needs.[13,14] These drawbacks make implementation of such technologies a cumbersome process, particularly for developing nations which bare the brunt of water scarcity issues.

Solar-driven desalination is a desirable alternative, where the sole energy input is sunlight.[15] Unfortunately, natural evaporation is a highly inefficient process due to the low absorption of water and intensive heat loss by non-evaporative processes.[16] To tackle these efficiency issues an influx of research has gone into discovering materials which can absorb broadband solar radiation and harness it to generate heat for water evaporation. Known as photothermal materials, the most prominent examples include non-radiative recombination in inorganic semiconductors,[17–20] thermal vibration in polymeric materials[21–23] and carbon-based light absorbers,[24–29] and localized heating in plasmonic nanostructures.[30,31] Plasmonic materials are perhaps the most promising as they display efficient light-to-heat conversion.[32–34] Under 1 sun illumination, top plasmonic materials have surpassed 90% solar-to-vapor conversion efficiency for saltwater.[35–42] A strong interplay of material design for efficient broadband absorption and heat conversion, along with device engineering to enhance thermal management, water supply and steam release is required for high solar-to-vapor conversion efficiency.[43–45] This has led to a vast library of materials, supports, and elaborate 3D evaporation scaffolds[46–49] for solar-vapor generation and desalination.[17,43,50–52] However, intricate designs can increase the cost of the evaporation interface and therefore, there is still room to enhance the evaporation rate and efficiency simply by finding a more suitable photothermal material and support.

Refractory plasmonic nanostructures composed of transition metal nitrides and carbides have emerged as promising and low-cost photothermal materials.[53,54] Our group and others have shown the utility of plasmonic nitrides for solar-driven desalination.[42,55,56] Similar to the nitrides, plasmonic group IV non-MXene carbides also exhibit strong photothermal properties,[57] however, they are relatively a newcomer in the field and haven't been widely explored. Recently, commercially purchased ZrC were used to develop a carbide solar-driven evaporator by Liu *et al*.[35] which showed evaporation rate and efficiency of 1.38 kg m^{-2} h^{-1} and 96%, respectively, under 1 sun illumination at a mass loading of 85 g m^{-2}. Herein, we report the performance of group IV plasmonic carbides (TiC, ZrC, and HfC) in solar vapor generation and desalination. The effect of carbide composition, particle loading, and salt concentration on evaporation performance was evaluated. Further, the influence of ambient humidity and temperature on the photothermal evaporation was studied.

Results and Discussion

Plasmonic group IV transition metal carbides (TMCs), TiC, ZrC, and HfC were prepared using a previously reported solid state procedure.[57] The metal oxide nanopowder (TiO_2, ZrO_2, or HfO_2) was reacted with birch-residue derived biochar and magnesium powder under argon atmosphere between 950 and 1100° C to yield corresponding carbides (TiC, ZrC, HfC). The biochar was synthesized via a reported pyrolysis method.[58] This synthesis method yields crystalline powders (Figure S1) consisting of polydisperse nanoparticles with an average diameter of 24, 31, and 42 nm for TiC, ZrC, and HfC samples, respectively (Figure S2). Detailed analyses done in a previous study have shown these nanoparticles also posses an amorphous oxide/oxycarbide shell around the crystalline carbide core.[57] To prepare the evaporation interface, a 1.0 mg mL^{-1} dispersion of a given TMC was dropcast onto a 2.5 cm diameter mixed cellulose ester (MCE) filter paper (0.45μm pore size) under vacuum to reach loadings of 0.5, 1.0, 1.5, and 2.0 g m^{-2}. The SEM images of the MCE filters with 1.0 g m^{-2} loading of the carbides (Figure 1A) showed that some degree of porosity is still retained after the coating. The TMC dispersions displayed absorbance maxima deep in the UV region (<200nm) as previously reported (Figure 1B),[57] and the absorbance of all three carbides approached zero at 800 nm. However, when loaded onto the MCE support, the absorbance broadened significantly. This led to average light absorption of 82% (ZrC), 86% (TiC), and 95% (HfC) between 300 and 1500 nm (Figure 1C). This broadband absorption likely originates from increased coupling of the plasmonic particles with one another while in close proximity on the MCE support[30,57,59] and could be further enhanced by light trapping within the pores.[60–62] The plasmonic TMC coated MCE filters were placed on top of a 0.5-inch EVA foam support with one dimensional cotton fabric wicks (Figure 1D). The EVA foam was used to provide thermal isolation of the carbide interface from the bulk water, while the root-like wick structure was used to provide ample water supply to the interface. The device has been adapted from various reports to provide efficient water transport while separating the interface from the bulk to minimize thermal losses.[30,32,34,43,44]

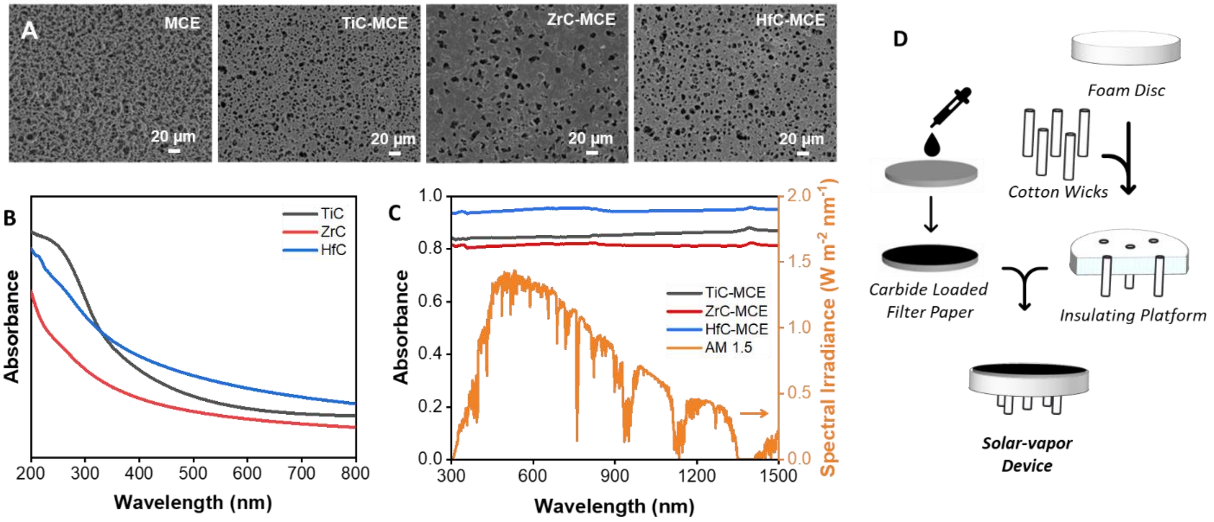

Figure 1: (A) Top-down SEM images of blank MCE filter and 1.0 g m^{-2} carbide loaded filters. Absorbance spectra of TMCs (B) as a dispersion in distilled water, and (C) loaded onto the MCE supports (left), with reference solar intensity spectrum for total global AM 1.5 radiation (orange, right). (D) Schematic illustration of carbide solar-vapor device fabrication.

To initially assess the solar-vapor generation potential of the TMCs, studies were carried out under one-sun illumination using a Pico^{TM} LED solar simulator and tap water. The relative humidity was maintained between 50-55% and ambient temperature was held at 22 °C. The plasmonic interfaces were floated onto water such that the edges of the foam left no gaps between itself and the container wall which minimized the possibility of any unaccounted evaporation from the surface of the water. The ambient evaporation rate (0.01 kg m^{-2} h^{-1}) was determined using dark studies and subtracted from the illuminated rates to account for natural evaporative process contributions. Finally, the evaporator surfaces were illuminated for 5 minutes to reach a steady state before measuring the temperature (Figure S3). The reported rate and efficiency values are averages from five trails.

The representative mass change plots for distilled water, blank solar-vapor device, and the metal carbide interfaces are shown in Figure 2A. The average evaporation rates for pure water and the blank MCE support were found to be 0.07 ± 0.01 and 0.38 ± 0.08 kg m^{-2} h^{-1}, respectively. For the carbide interfaces, mass loadings of 0.5, 1.0, 1.5, and 2.0 g m^{-2} were investigated, and 1.0 g m^{-2} was found to be the best performing (Figure S4). At lower loadings, the surface coverage is low, thereby decreasing the efficiency as reflection off the MCE filter becomes an issue. On the other hand, higher loads block the pores of the MCE support, hindering the release of water vapor (Figure S5). The 1.0 g m^{-2} mass loading is likely the optimum value which falls in between these two scenarios, yielding a maximum evaporation rate for the MCE filters used. For the optimized TMC loadings, ZrC had the lowest evaporation rate of 1.22 ± 0.04 kg m^{-2} h^{-1}, followed by TiC (1.31 ± 0.01 kg m^{-2} h^{-1}). HfC had the highest evaporation rate in the series with an average value of 1.41 ± 0.02 kg m^{-2} h^{-1}. The resulting solar-to-vapor efficiency was evaluated for each sample using a previously reported equation (1),

$$\eta = \nu \frac{C\Delta T + \Delta_{vap}H_m}{C_{opt}q_i} \tag{1}$$

where v is the evaporation rate, C is the specific heat capacity of water (4.18 kJ kg^{-1} K^{-1}, ΔT is the change in temperature, $\Delta_{vap}H_m$ is the liquid to vapor phase change enthalpy of water, C_{opt} is the optical concentration, and q_i is the illumination intensity of the light in kW m^{-2}. HfC interfaces had the highest solar-to-vapor efficiency value of 97% followed by TiC and ZrC with efficiencies of 89% and 86%, respectively (Figure 2B). The efficiency trend follows the light absorption capability of TMC interfaces with HfC absorbing the most amount followed by TiC and ZrC, respectively (Figure 1C).

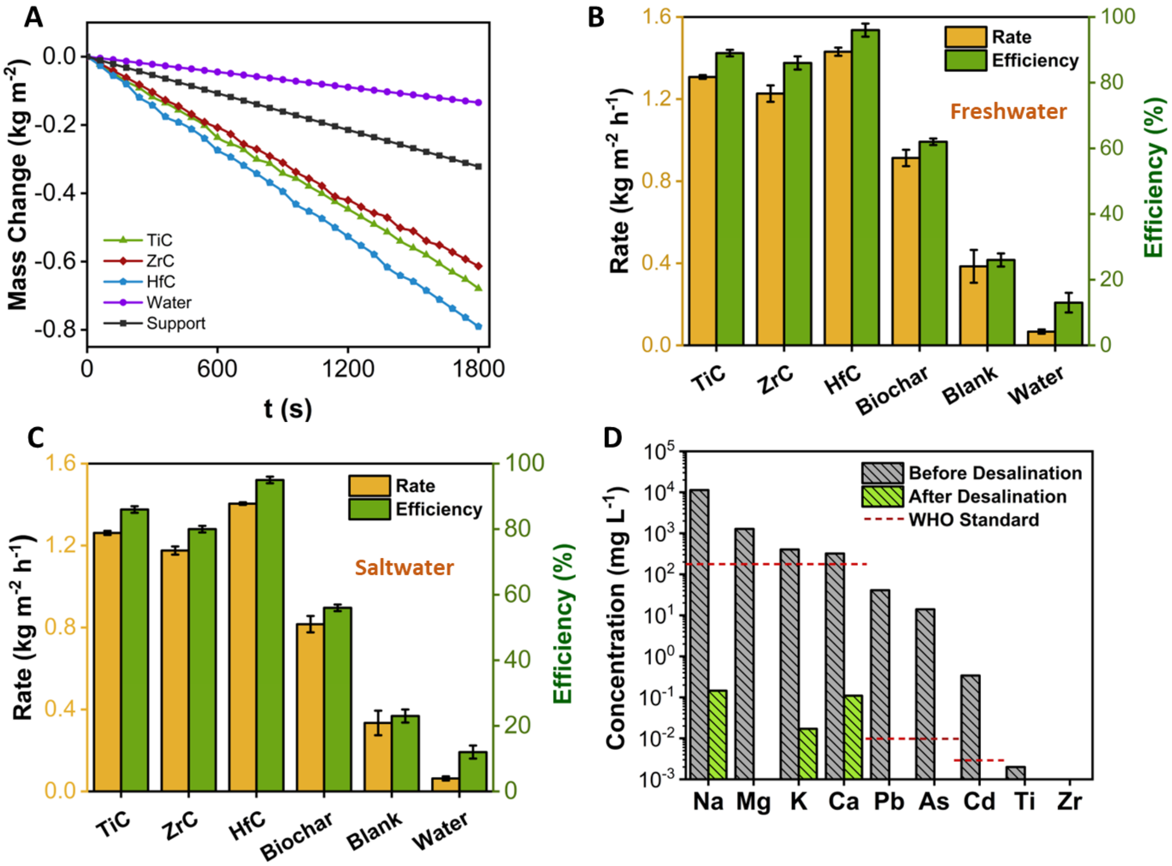

Figure 2: (A) Mass change plots for the carbide, biochar, blank supports, and water under 1-sun illumination. Rates (blue, left) and corresponding solar-to-vapor conversion efficiencies (green, right) for (B) freshwater and (C) saltwater. (D) Metal analysis by ICP MS for water before (grey striped) and after (green striped) desalination using TiC interface.

To demonstrate the potential for freshwater generation, the desalination capabilities of the metal carbide interfaces were investigated using saltwater obtained from the Atlantic Ocean. Under 1-sun illumination, HfC once again performed the best with an evaporation rate of 1.40 ± 0.01 kg m^{-2} h^{-1}, however, TiC and ZrC saw a decrease in performance compared to the freshwater evaporation rates to 1.26 ± 0.01 and 1.18 ± 0.02 kg m^{-2} h^{-1}, respectively. This represents desalination solar-to-vapor conversion efficiencies of 86, 80, and 96% for TiC, ZrC, and HfC, respectively (Figure 2C). The biochar used to synthesize carbides was also explored for the evaporation experiments. For both fresh and saltwater, the biochar interface had a lower evaporation rate of 0.91 ± 0.04, and 0.82 ± 0.04 kg m^{-2} h^{-1}, respectively. While carbon materials such as biochar can be directly used for evaporation, these results highlight the enhanced photothermal properties of plasmonic materials for solar steam generation. Metal analysis was performed using inductively coupled plasma mass spectrometry (ICP-MS) on desalinated water and for the TiC a decrease in salt ion concentrations by 3-5 orders of magnitude was observed (Figure 2D), dropping them well below the standards set by the World Health Organization (WHO). Additionally, samples were tested for metals in TMC to show that there is no leaching of metals from the carbide interface (Figure 2D). ICP-MS results for the desalinated water obtained using ZrC and HfC interfaces can be seen in Figure S6, where the concentration of metal ions is similar to those of TiC.

The performance of the TMCs were compared to similar interfaces reported in the literature that demonstrated solar-driven saltwater evaporation. Aminosilane functionalized ZrC nanoparticles on MCE paper displayed a desalination rate of 1.38 kg m^{-2} h^{-1} under 1-sun illumination, however, a high mass loading of 85 g m^{-2} was required to reach this rate.[35] MXene phase Ti_3C_2 on multi-walled carbon nanotubes (MWCNT) were vacuum loaded onto MCE paper (mass loading of 2.0 g m^{-2}) which had a desalination rate of 1.32 kg m^{-2} h^{-1}.[36] Our group previously reported HfN interfaces capable of desalinating at 1.20 kg m^{-2} h^{-1} with a mass loading of 2.5 g m^{-2}.[38] Table S1 shows a comparison of some top-performing materials for solar desalination under 1-sun illumination. The HfC interface reported here outperforms these materials and has a lower mass loading than previous reports. It should be noted that 3D evaporation structure or cross-linked polymer supports, where cluster evaporation[44,63] or hydrogen bond disruption[48,64] can lower the required enthalpy of vaporization, resulting in high evaporation rates. Incorporation of plasmonic refractory materials in such designs can potentially result in higher rates than those currently reported. [44, 48, 63–65]

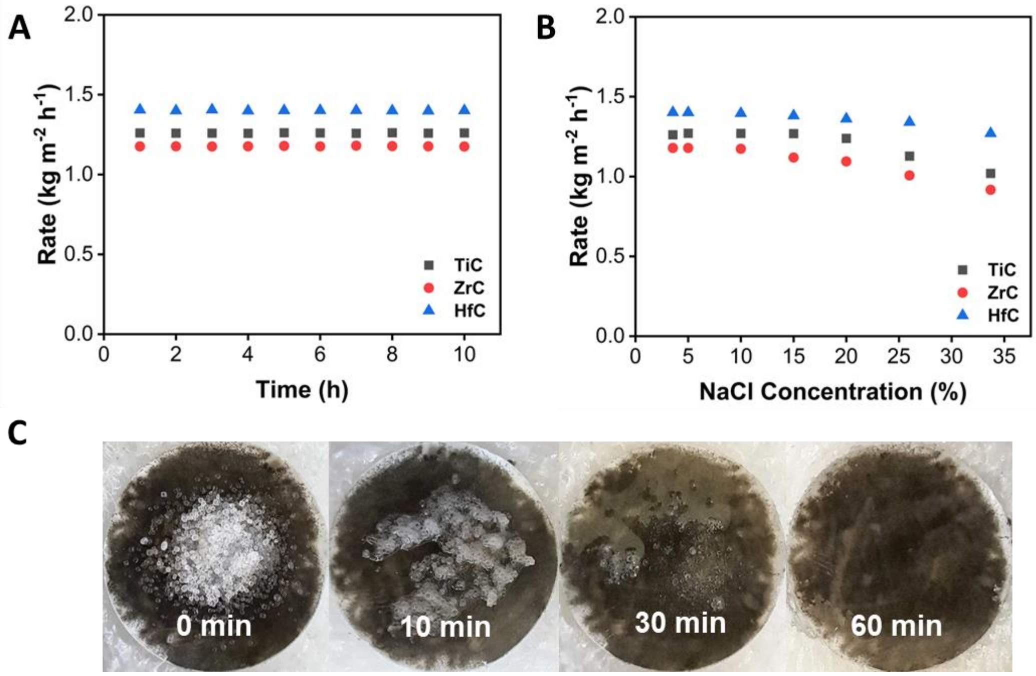

Figure 3: (A) Evaporation rates after each hour of illumination over the course of 10 straight hours of desalination using TMC interfaces. (B) Evaporation rates for different salt concentrations using TMC interfaces under 1-sun illumination. (C) Dissolution of salt from the surface of TiC desalination interface over time.

The stability of TMC interfaces were tested over the course of 10 hours and the rate of evaporation remained unchanged (Figure 3A). This highlights the ability of the root-like wick structure to effectively avoid salt buildup on the surface which can occur in porous alumina substrates.[38] To further explore the salt tolerance and rejection capability of these interfaces, NaCl solutions with concentrations ranging from 3.5 – 35% were tested. The HfC maintained its original evaporation rate of 1.40 kg m^{-2} h^{-1} up to 10% solution and decreased to 1.27 kg m^{-2} h^{-1} in the presence of 35% NaCl solution (Figure 3B). Similar to HfC, the TiC and ZrC maintained their evaporation performance for NaCl concentrations up to 10%. However, with increasing NaCl amounts a rate drop of 0.24 and 0.26 kg m^{-2} h^{-1} was observed for TiC and ZrC, respectively, which is higher than HfC. In addition to higher evaporation rates and efficiencies, HfC demonstrates better tolerance to high salt concentrations. The ability of these interfaces to avoid salt buildup is illustrated by its dissolution experiments. NaCl crystals were placed on the TiC interface (time 0, Figure 3C) and illuminated for an hour and over time the salt is dissolved and removed from the interface (time 60 min, Figure 3C).

As seen in Table S1, the relative humidity and temperature can vary from lab to lab and also in the real-world setting. In order to perform solar-driven desalination, it is important to understand how differences in such conditions can affect evaporation rates and efficiencies. Therefore, a series of experiments were conducted to study the influence of ambient temperature and relative humidity on the evaporation process using the TMC interfaces. To study the thermal effect, the room temperature was varied between 15 – 30 °C with constant humidity (50%). For relative humidity studies, the temperature was held constant (22 °C), and the humidity was varied between 20 – 80%. The evaporation rates increased with increasing ambient temperature, as the bulk water now requires less additional energy input to make the liquid to vapor transition. While the TiC and ZrC interfaces showed a linear increase across the entire temperature range, HfC levels off at higher temperatures. This is likely due to the rate of evaporation reaching the theoretical limit defined by the enthalpy of vaporization for water.[65] A rate change of 0.0080, 0.0060, and 0.0050 kg m^{-2} h^{-1} $°C^{-1}$ was observed for ambient temperature change for TiC, ZrC, and HfC, respectively with a corresponding efficiency increase of 5 – 8% over range tested. Variations in relative humidity was also found to influence the recorded rates of desalination. The rates changed by 0.0024, 0.0024, and 0.00060 kg m^{-2} h^{-1} per percent humidity for TiC, ZrC, and HfC, respectively. Previous numerical studies have predicted a linear drop in evaporation performance with increasing relative humidity as observed here due to the higher moisture content of the air suppressing evaporation.[66]

While TiC and ZrC showed comparable drop in the evaporation rates, HfC interfaces were affected to a lesser extent. This highlights the importance of monitoring such evaporation conditions for reporting and holding them steady between trials.

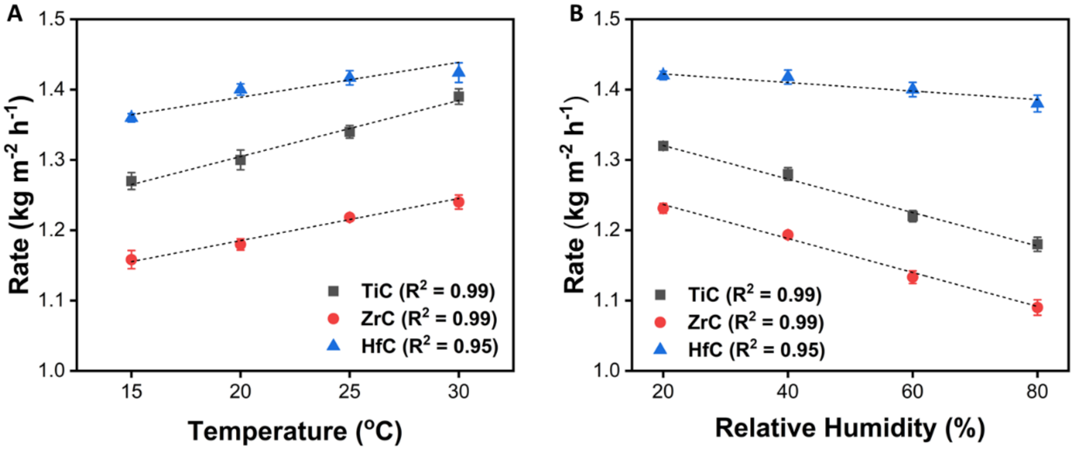

Figure 4: Influence of (A) ambient temperature and (B) relative humidity on the evaporation rates for TMC interfaces.

Conclusions

To examine the potential of plasmonic TMC nanomaterials for solar-vapor generation and desalination, they were synthesized using a solid-state method and loaded onto MCE membranes. Under 1 sun illumination and at a mass loading of 1.0 g m^{-2}, HfC interfaces were found to perform the best with evaporation rate and efficiency of 1.40 ± 0.01 kg m^{-2} h^{-1} and 96%, respectively. Effective removal of common metal ion contaminants was displayed post desalination, with levels 2-3 orders of magnitude below World Health Organization standards. The carbide interfaces successfully rejected salt over time, therefore maintaining evaporation performance and can desalinate under hypersaline conditions up to 35% NaCl. HfC interfaces were also less susceptible to changes in the salt concentrations, ambient temperatures, and relative humidity compared to

TiC and ZrC. Overall, group IV TMC nanomaterials represent a promising class of solar desalination materials, with potential for facile scaling up of the interfaces.

Experimental

Materials

Titanium dioxide (TiO_2, 99.9%, 18 nm), zirconium dioxide (ZrO_2, 99.9%, 20 nm), and hafnium dioxide (HfO_2, 99.9%, 61-80 nm) were purchased from U.S. Research Nanomaterials. Magnesium powder (Mg, 99.8%, 325 mesh) was purchased from Alfa Aesar. Hydrochloric acid (HCl, $\geq$ 99%) and nitric acid (HNO_3, $\geq$ 99%) were purchased from Sigma Aldrich. Deionized water (DI water, 18.2 MΩ cm) was obtained from Sartorius Arium water purification system. Mixed cellulose ester filters (MCE, 0.45 μm pore size, 25 mm) were purchased from Cole Parmer. Saltwater was obtained from the Atlantic Ocean (coordinates: 44°38’23.7”N 63°36’48.0”W).

Synthesis of Biochar

Biochar was prepared using a previously reported anaerobic pyrolysis process.[58] Briefly, birch wood residue was pyrolyzed at 400 °C for 30 minutes under an N_2 atmosphere and quenched in cold water. The biochar was then washed in boiling distilled water for 15 min. The biochar was collected via filtration and the solid product was washed with water until the filtrate ran clear. The resulting biochar was dried, ground, and finally sieved to a particle size of ~150 μm. The sieved biochar was then added to a beaker equipped with a magnetic stir-bar and reacted with concentrated HNO_3 for 30 minutes. Afterwards, the reaction was filtered, and the acid-treated biochar was rinsed with deionized water until the filtrate was neutral. The biochar was dried in an oven at 100 °C for 2 days.

Synthesis of Metal Carbide Nanoparticles

The metal carbides were prepared according to a previously reported procedure.[57] Briefly, in a nitrogen filled glovebox, 0.50 g of the corresponding metal oxide (TiO_2 ZrO_2, or HfO_2) was mixed with biochar (2 molar excess to the metal oxide) and magnesium (4 molar excess to the metal oxide) powders using a mortar and pestle until a homogenous mixture was obtained. The mixtures were transferred to a Coors™ alumina combustion boat and placed into a quartz tube. After purging with argon gas for 15 min in a Lindberg Blue MTM furnace, the mixtures were heated to either 950 °C (TiC, ZrC), or 1100 ˚C (HfC) at a ramp rate of 10 °C min^{-1} and held at those temperatures for 4 hours. The reaction mixture was cooled to ambient temperature and transferred to a glass beaker. 6.0 M HCl (20 mL) was added to the reaction product and was sonicated for 1 hour. Carbides were washed in distilled water (3 x 10 mL) by sonication, centrifugation, and pouring off of the supernatant each time. After the third wash, the carbides were filtered and rinsed with acetone, followed by ethanol, then dried in an oven.

Plasmonic Evaporation Interface Fabrication

Plasmonic metal carbide (TiC, ZrC, or HfC) interfaces were prepared by vacuum-loading a given volume of 1.0 g mL^{-1} solution of carbide onto a 25 mm diameter MCE filter (Cole Parmer, pore size 0.45 μm) for a loading of either 0.5, 1.0, 1.5, or 2.0 g·m^2. The plasmonic carbide filter paper was then placed onto a foam disc (polypropylene, 2.5 cm diameter x 1 cm thick) with 1D fabric wicks (Zorb®) inserted into the foam (Figure 1A).

Water Evaporation Experiments

Evaporation experiments (freshwater and saltwater) were performed using a solar simulator (Pico™ Small Area LED, G2V). Mass change was recorded to a computer directly connected to a calibrated analytical balance (VWR-164AC) using CoolTerm (Roger Meier). The plasmonic evaporation platform was floated on top of water in a small glass beaker. The interface was illuminated from above and the mass change was measured over 10 minutes with data points being collected every 5 seconds. Before starting runs, the interface was illuminated for 5 minutes to reach a steady temperature. Temperature was recorded using an infrared thermal camera (Perfect Prime IR0005). Ambient temperature was maintained at 22 °C for experiments, and relative humidity was between 50 – 55% for the trials. For variable temperature and humidity studies, a polyethylene and PVC pipe chamber was constructed with temperature and humidity controls connected to a ceramic heater or a humidifier, respectively. Metal ion concentration samples were collected using an enclosed quartz vessel with a slanted cover and a separate collection chamber.

Characterization Methods

Powder X-ray diffraction (XRD) spectra were collected using a Proto AXRD® Benchtop with a Cu Kα radiation (λ = 1.54 Å). Powders were packed into a sample well of a resin holder. Absorbance and reflectance spectra were recorded on an Agilent CARY 5000 UV-Vis-NIR spectrometer. For liquid absorbance measurements, dispersions were placed into a quartz cuvette, and the spectrometer was background corrected using deionized water. For film samples, an external diffuse reflectance accessory with a 150 mm integrating sphere was used. The instrument was used in double beam mode using reduced slit height and was standard calibrated using a zero/baseline correction. Transmission electron microscopy (TEM) images were collected using a Thermo Fisher Scientific Talos 200X microscope with an accelerating voltage of 200 kV. Scanning electron microscopy (SEM) images were obtained on a Hitachi S-4700 electron microscope. Inductively coupled plasma mass spectrometry (ICP-MS) measurements were performed on a Thermo Scientific X-Series 2 spectrometer and the standards were obtained from SCP Science.

ASSOCIATED CONTENT

Electronic Supplementary Information.

Powder XRD patterns and TEM images of TiC, ZrC, and HfC NPs. Representative infrared thermal images of the MCE and TMC interfaces. Representative SEM images of TiC interfaces at different mass loadings. Evaporation rates for TMC interfaces at different mass loadings. ICP-MS analysis of desalinated water from ZrC and HfC interfaces. Summary of the performance of other water evaporation interfaces reported in the literature with design comparable to that reported here.

Conflicts of interest

There are no conflicts to declare.

Corresponding Author

*Email: mita.dasog@dal.ca

Acknowledgements

The authors thank funding from the Natural Sciences and Engineering Research Council of Canada Discovery Grant, Canada Foundation for Innovation, and Ocean Frontier Institute. MA thanks Joy M. Cunningham endowment for Research Award and and MM for graduate fellowship from Sumner Foundation. Dr. Sarah Martell and the Clean Technologies Research Institute are thanked for access and assistance with the SEM analysis. Dr. Carmen Andrei and Canadian Center for Microscopy are thanked for assistance with the TEM and EDS mapping experiments. Dr.

Heather Andreas is thanked for access to the UV-Vis-NIR absorbance spectrometer. Dr. Graham Gagnon and Heather Daurie are thanked for the assistance with ICP-MS measurements.

References

(1) Kummu, M.; Guillaume, J. H. A.; de Moel, H.; Eisner, S.; Flörke, M.; Porkka, M.; Siebert, S.; Veldkamp, T. I. E.; Ward, P. J. The World's Road to Water Scarcity: Shortage and Stress in the 20th Century and Pathways towards Sustainability. *Sci. Rep.* **2016**, *6* (1), 38495. https://doi.org/10.1038/srep38495.

(2) Veldkamp, T. I. E.; Wada, Y.; Aerts, J. C. J. H.; Döll, P.; Gosling, S. N.; Liu, J.; Masaki, Y.; Oki, T.; Ostberg, S.; Pokhrel, Y.; Satoh, Y.; Kim, H.; Ward, P. J. Water Scarcity Hotspots Travel Downstream Due to Human Interventions in the 20th and 21st Century. *Nat. Commun.* **2017**, *8* (1), 15697. https://doi.org/10.1038/ncomms15697.

(3) Boretti, A.; Rosa, L. Reassessing the Projections of the World Water Development Report. *NPJ Clean Water.* **2019**, *2* (1), 15. https://doi.org/10.1038/s41545-019-0039-9.

(4) He, L.; Rosa, L. Solutions to Agricultural Green Water Scarcity under Climate Change. *PNAS Nexus.* **2023**, *2* (4), pgad117. https://doi.org/10.1093/pnasnexus/pgad117.

(5) Martin-Carrasco, F.; Garrote, L.; Iglesias, A.; Mediero, L. Diagnosing Causes of Water Scarcity in Complex Water Resources Systems and Identifying Risk Management Actions. *Water Res. Manag.* **2013**, *27* (6), 1693–1705. https://doi.org/10.1007/s11269-012-0081-6.

(6) Elimelech, M.; Phillip, W. A. The Future of Seawater Desalination: Energy, Technology, and the Environment. *Science.* **2011**, *333* (6043), 712–717. https://doi.org/10.1126/science.1200488.

(7) Khawaji, A. D.; Kutubkhanah, I. K.; Wie, J.-M. Advances in Seawater Desalination Technologies. *Desalination.* **2008**, *221* (1), 47–69. https://doi.org/https://doi.org/10.1016/j.desal.2007.01.067.

(8) Sharaf, M. A.; Nafey, A. S.; García-Rodríguez, L. Thermo-Economic Analysis of Solar Thermal Power Cycles Assisted MED-VC (Multi Effect Distillation-Vapor Compression) Desalination Processes. *Energy.* **2011**, *36* (5), 2753–2764. https://doi.org/https://doi.org/10.1016/j.energy.2011.02.015.

(9) Zhao, D.; Xue, J.; Li, S.; Sun, H.; Zhang, Q. Theoretical Analyses of Thermal and Economical Aspects of Multi-Effect Distillation Desalination Dealing with High-Salinity Wastewater. *Desalination.* **2011**, *273* (2), 292–298. https://doi.org/https://doi.org/10.1016/j.desal.2011.01.048.

(10) Greenlee, L. F.; Lawler, D. F.; Freeman, B. D.; Marrot, B.; Moulin, P. Reverse Osmosis Desalination: Water Sources, Technology, and Today's Challenges. *Water Res.* **2009**, *43* (9), 2317–2348. https://doi.org/https://doi.org/10.1016/j.watres.2009.03.010.

(11) Peñate, B.; García-Rodríguez, L. Current Trends and Future Prospects in the Design of Seawater Reverse Osmosis Desalination Technology. *Desalination.* **2012**, *284*, 1–8. https://doi.org/https://doi.org/10.1016/j.desal.2011.09.010.

(12) Qasim, M.; Badrelzaman, M.; Darwish, N. N.; Darwish, N. A.; Hilal, N. Reverse Osmosis Desalination: A State-of-the-Art Review. *Desalination.* **2019**, *459*, 59–104. https://doi.org/https://doi.org/10.1016/j.desal.2019.02.008.

(13) AlSawaftah, N.; Abuwatfa, W.; Darwish, N.; Husseini, G. A Comprehensive Review on Membrane Fouling: Mathematical Modelling, Prediction, Diagnosis, and Mitigation. *Water.* **2021**, *13* (9). https://doi.org/10.3390/w13091327.

(14) Najid, N.; Fellaou, S.; Kouzbour, S.; Gourich, B.; Ruiz-García, A. Energy and Environmental Issues of Seawater Reverse Osmosis Desalination Considering Boron Rejection: A Comprehensive Review and a Case Study of Exergy Analysis. *Process Saf. Environ. Prot.* **2021**, *156*, 373–390. https://doi.org/https://doi.org/10.1016/j.psep.2021.10.014.

(15) Ghaffour, N.; Bundschuh, J.; Mahmoudi, H.; Goosen, M. F. A. Renewable Energy-Driven Desalination Technologies: A Comprehensive Review on Challenges and Potential Applications of Integrated Systems. *Desalination.* **2015**, *356*, 94–114. https://doi.org/https://doi.org/10.1016/j.desal.2014.10.024.

(16) Xu, N.; Li, J.; Finnerty, C.; Song, Y.; Zhou, L.; Zhu, B.; Wang, P.; Mi, B.; Zhu, J. Going beyond Efficiency for Solar Evaporation. *Nature Water.* **2023**, *1* (6), 494–501. https://doi.org/10.1038/s44221-023-00086-5.

(17) Ibrahim, I.; Seo, D. H.; McDonagh, A. M.; Shon, H. K.; Tijing, L. Semiconductor Photothermal Materials Enabling Efficient Solar Steam Generation toward Desalination and Wastewater Treatment. *Desalination.* **2021**, *500*, 114853. https://doi.org/https://doi.org/10.1016/j.desal.2020.114853.

(18) Tan, K. W.; Yap, C. M.; Zheng, Z.; Haw, C. Y.; Khiew, P. S.; Chiu, W. S. State-of-the-Art Advances, Development, and Challenges of Metal Oxide Semiconductor Nanomaterials for Photothermal Solar Steam Generation. *Adv. Sustain. Syst.* **2022**, *6* (4), 2100416. https://doi.org/https://doi.org/10.1002/adsu.202100416.

(19) El-Sapa, S.; El-Bary, A. A.; Chtioui, H.; Becheikh, N.; Lotfy, K. Photothermal Excitation in Non-Local Semiconductor Materials with Variable Moisture Thermal Conductivity According to Moisture Diffusivity. *Front. Mater.* **2023**, *10*. https://doi.org/10.3389/fmats.2023.1193423.

(20) Cui, X.; Ruan, Q.; Zhuo, X.; Xia, X.; Hu, J.; Fu, R.; Li, Y.; Wang, J.; Xu, H. Photothermal Nanomaterials: A Powerful Light-to-Heat Converter. *Chem. Rev.* **2023**, *123* (11), 6891–6952. https://doi.org/10.1021/acs.chemrev.3c00159.

(21) Chen, P.; Ma, Y.; Zheng, Z.; Wu, C.; Wang, Y.; Liang, G. Facile Syntheses of Conjugated Polymers for Photothermal Tumour Therapy. *Nat. Commun.* **2019**, *10* (1), 1192. https://doi.org/10.1038/s41467-019-09226-6.

(22) Xiao, L.; Chen, X.; Yang, X.; Sun, J.; Geng, J. Recent Advances in Polymer-Based Photothermal Materials for Biological Applications. *ACS Appl. Polym. Mater.* **2020**, *2* (10), 4273–4288. https://doi.org/10.1021/acsapm.0c00711.

(23) Wang, M.; Huang, X.; Yang, H. Photothermal-Responsive Crosslinked Liquid Crystal Polymers. *Macromol. Mater. Eng.* **2023**, 2300061. https://doi.org/https://doi.org/10.1002/mame.202300061.

(24) Yang, H.-C.; Chen, Z.; Xie, Y.; Wang, J.; Elam, J. W.; Li, W.; Darling, S. B. Chinese Ink: A Powerful Photothermal Material for Solar Steam Generation. *Adv. Mater. Interfaces.* **2019**, *6* (1), 1801252. https://doi.org/https://doi.org/10.1002/admi.201801252.

(25) Liu, H.; Huang, G.; Wang, R.; Huang, L.; Wang, H.; Hu, Y.; Cong, G.; Bao, F.; Xu, M.; Zhu, C.; Xu, J.; Ji, M. Carbon Nanotubes Grown on the Carbon Fibers to Enhance the Photothermal Conversion toward Solar-Driven Applications. *ACS Appl. Mater. Interfaces.* **2022**, *14* (28), 32404–32411. https://doi.org/10.1021/acsami.2c07970.

(26) Xie, Z.; Wang, H.; Geng, Y.; Li, M.; Deng, Q.; Tian, Y.; Chen, R.; Zhu, X.; Liao, Q. Carbon-Based Photothermal Superhydrophobic Materials with Hierarchical Structure Enhances the Anti-Icing and Photothermal Deicing Properties. *ACS Appl. Mater. Interfaces.* **2021**, *13* (40), 48308–48321. https://doi.org/10.1021/acsami.1c15028.

(27) Qi, K.; Sun, B.; Liu, S.; Zhang, M. Research Progress on Carbon Materials in Tumor Photothermal Therapy. *Biomed. Pharmacother.* **2023**, *165*, 115070. https://doi.org/https://doi.org/10.1016/j.biopha.2023.115070.

(28) Yang, T.; Lin, H.; Lin, K.-T.; Jia, B. Carbon-Based Absorbers for Solar Evaporation: Steam Generation and Beyond. *Sus. Mater. and Tech.* **2020**, *25*, e00182. https://doi.org/https://doi.org/10.1016/j.susmat.2020.e00182.

(29) Dao, V.-D.; Choi, H.-S. Carbon-Based Sunlight Absorbers in Solar-Driven Steam Generation Devices. *Global Chall.* **2018**, *2* (2), 1700094. https://doi.org/https://doi.org/10.1002/gch2.201700094.

(30) Liang, J.; Liu, H.; Yu, J.; Zhou, L.; Zhu, J. Plasmon-Enhanced Solar Vapor Generation. *Nanophotonics.* **2019**, *8* (5), 771–786. https://doi.org/doi:10.1515/nanoph-2019-0039.

(31) Deng, Z.; Zhou, J.; Miao, L.; Liu, C.; Peng, Y.; Sun, L.; Tanemura, S. The Emergence of Solar Thermal Utilization: Solar-Driven Steam Generation. *J. Mater. Chem. A* **2017**, *5* (17), 7691–7709. https://doi.org/10.1039/C7TA01361B.

(32) Zhou, L.; Li, X.; Ni, G. W.; Zhu, S.; Zhu, J. The Revival of Thermal Utilization from the Sun: Interfacial Solar Vapor Generation. *Natl. Sci. Rev.* **2019**, *6* (3), 562–578. https://doi.org/10.1093/nsr/nwz030.

(33) Zhao, F.; Guo, Y.; Zhou, X.; Shi, W.; Yu, G. Materials for Solar-Powered Water Evaporation. *Nat. Rev. Mater.* **2020**, *5* (5), 388–401. https://doi.org/10.1038/s41578-020-0182-4.

(34) Min, X.; Zhu, B.; Li, B.; Li, J.; Zhu, J. Interfacial Solar Vapor Generation: Materials and Structural Design. *Acc. Mater. Res.* **2021**, *2* (4), 198–209. https://doi.org/10.1021/accountsmr.0c00104.

(35) Ai, S.; Ma, M.; Chen, Y.-Z.; Gao, X.-H.; Liu, G. Metal-Ceramic Carbide Integrated Solar-Driven Evaporation Device Based on ZrC Nanoparticles for Water Evaporation and Desalination. *Chem. Eng. J.* **2022**, *429*, 132014. https://doi.org/https://doi.org/10.1016/j.cej.2021.132014.

(36) Yang, Y.; Han, Y.; Zhao, J.; Que, W. 2D/1D MXene/MWCNT Hybrid Membrane-Based Evaporator for Solar Desalination. *Materials.* **2022**, *15* (3), 929. https://doi.org/10.3390/ma15030929.

(37) Huang, H.; Zhao, L.; Yu, Q.; Lin, P.; Xu, J.; Yin, X.; Chen, S.; Wang, H.; Wang, L. Flexible and Highly Efficient Bilayer Photothermal Paper for Water Desalination and Purification: Self-Floating, Rapid Water Transport, and Localized Heat. *ACS Appl. Mater. Interfaces.* **2020**, *12* (9), 11204–11213. https://doi.org/10.1021/acsami.9b22338.

(38) Traver, E.; Karaballi, R. A.; Monfared, Y. E.; Daurie, H.; Gagnon, G. A.; Dasog, M. TiN, ZrN, and HfN Nanoparticles on Nanoporous Aluminum Oxide Membranes for Solar-Driven Water Evaporation and Desalination. *ACS Appl. Nano. Mater.* **2020**, *3* (3), 2787–2794. https://doi.org/10.1021/acsanm.0c00107.

(39) Chang, C.; Liu, M.; Pei, L.; Chen, G.; Wang, Z.; Ji, Y. Porous TiNO Solar-Driven Interfacial Evaporator for High-Efficiency Seawater Desalination. *AIP Adv.* **2021**, *11* (4), 045228. https://doi.org/10.1063/5.0047390.

(40) Liu, Y.; Liu, Z.; Huang, Q.; Liang, X.; Zhou, X.; Fu, H.; Wu, Q.; Zhang, J.; Xie, W. A High-Absorption and Self-Driven Salt-Resistant Black Gold Nanoparticle-Deposited Sponge for Highly Efficient, Salt-Free, and Long-Term Durable Solar Desalination. *J. Mater. Chem. A* **2019**, *7* (6), 2581–2588. https://doi.org/10.1039/C8TA10227A.

(41) Qin, Y.; Li, Y.; Wu, R.; Wang, X.; Qin, J.; Fu, Y.; Qin, M.; Wang, Z.; Zhang, Y.; Zhang, F. Bilayer Designed Paper-Based Solar Evaporator for Efficient Seawater Desalination. *Nanomaterials.* **2022**, *12* (19), 3487. https://doi.org/10.3390/nano12193487.

(42) Farid, M. U.; Kharraz, J. A.; Wang, P.; An, A. K. High-Efficiency Solar-Driven Water Desalination Using a Thermally Isolated Plasmonic Membrane. *J. Clean Prod.* **2020**, *271*, 122684. https://doi.org/https://doi.org/10.1016/j.jclepro.2020.122684.

(43) Gu, X.; Fan, C.; Sun, Y. Multilevel Design Strategies of High-Performance Interfacial Solar Vapor Generation: A State-of-the-Art Review. *Chem. Eng. J.* **2023**, *460*, 141716. https://doi.org/https://doi.org/10.1016/j.cej.2023.141716.

(44) Yu, S.; Gu, Y.; Chao, X.; Huang, G.; Shou, D. Recent Advances in Interfacial Solar Vapor Generation: Clean Water Production and Beyond. *J. Mater. Chem. A.* **2023**, *11* (12), 5978–6015. https://doi.org/10.1039/D2TA10083E.

(45) Wei, D.; Wang, C.; Zhang, J.; Zhao, H.; Asakura, Y.; Eguchi, M.; Xu, X.; Yamauchi, Y. Water Activation in Solar-Powered Vapor Generation. *Adv. Mater.* **2023**, *accepted*, 2212100. https://doi.org/https://doi.org/10.1002/adma.202212100.

(46) Wang, Z.; Liu, H.; Chen, F.; Zhang, Q. A Three-Dimensional Printed Biomimetic Hierarchical Graphene Architecture for High-Efficiency Solar Steam-Generation. *J. Mater. Chem. A.* **2020**, *8* (37), 19387–19395. https://doi.org/10.1039/D0TA06797K.

(47) Gao, T.; Wu, X.; Wang, Y.; Owens, G.; Xu, H. A Hollow and Compressible 3D Photothermal Evaporator for Highly Efficient Solar Steam Generation without Energy Loss. *Solar RRL.* **2021**, *5* (5), 2100053. https://doi.org/https://doi.org/10.1002/solr.202100053.

(48) Alketbi, A. S.; Raza, A.; Sajjad, M.; Li, H.; AlMarzooqi, F.; Zhang, T. Direct Solar Vapor Generation with Micro-3D Printed Hydrogel Device. *EcoMat.* **2022**, *4* (1), e12157. https://doi.org/https://doi.org/10.1002/eom2.12157.

(49) Liu, Y.; Luo, B.; Liu, H.; He, M.; Wang, R.; Wang, L.; Quan, Z.; Yu, J.; Qin, X. 3D Printed Electrospun Nanofiber-Based Pyramid-Shaped Solar Vapor Generator with Hierarchical Porous Structure for Efficient Desalination. *Chem. Eng. J.* **2023**, *452*, 139402. https://doi.org/https://doi.org/10.1016/j.cej.2022.139402.

(50) Kaviti, A. K.; Sri Ganesh Balaji, J.; Siva Ram, A.; Aruna Kumari, A. An Overview on Hydrogel Materials for Solar Desalination. *Mater. Today Proc.* **2021**, *44*, 2526–2532. https://doi.org/https://doi.org/10.1016/j.matpr.2020.12.604.

(51) Zang, L.; Finnerty, C.; Zheng, S.; Conway, K.; Sun, L.; Ma, J.; Mi, B. Interfacial Solar Vapor Generation for Desalination and Brine Treatment: Evaluating Current Strategies of Solving Scaling. *Water Res.* **2021**, *198*, 117135. https://doi.org/https://doi.org/10.1016/j.watres.2021.117135.

(52) Hu, X.; Zhu, J. Tailoring Aerogels and Related 3D Macroporous Monoliths for Interfacial Solar Vapor Generation. *Adv. Funct. Mater.* **2020**, *30* (3), 1907234. https://doi.org/https://doi.org/10.1002/adfm.201907234.

(53) Zhang, X.; Shao, J.; Yan, C.; Qin, R.; Lu, Z.; Geng, H.; Xu, T.; Ju, L. A Review on Optoelectronic Device Applications of 2D Transition Metal Carbides and Nitrides. *Mater. Des.* **2021**, *200*, 109452. https://doi.org/https://doi.org/10.1016/j.matdes.2021.109452.

(54) Dasog, M. Transition Metal Nitrides Are Heating Up the Field of Plasmonics. *Chemistry of Materials.* **2022**, *34* (10), 4249–4258. https://doi.org/10.1021/acs.chemmater.2c00305.

(55) Bricchi, B. R.; Mascaretti, L.; Garattoni, S.; Mazza, M.; Ghidelli, M.; Naldoni, A.; Li Bassi, A. Nanoporous Titanium (Oxy)Nitride Films as Broadband Solar Absorbers. *ACS Appl. Mater. Interfaces* **2022**, *14* (16), 18453–18463. https://doi.org/10.1021/acsami.2c01185.

(56) Mascaretti, L.; Schirato, A.; Zbořil, R.; Kment, Š.; Schmuki, P.; Alabastri, A.; Naldoni, A. Solar Steam Generation on Scalable Ultrathin Thermoplasmonic TiN Nanocavity Arrays.

Nano Energy. **2021**, *83*, 105828. https://doi.org/https://doi.org/10.1016/j.nanoen.2021.105828.

(57) Margeson, M. J.; Monfared, Y. E.; Dasog, M. Synthesis and Photothermal Properties of UV-Plasmonic Group IV Transition Metal Carbide Nanoparticles. *ACS App. Opt. Mater.* **2023**, *1* (5), 1004–1011. https://doi.org/10.1021/acsaom.3c00073.

(58) Humagain, G.; MacDougal, K.; MacInnis, J.; Lowe, J. M.; Coridan, R. H.; MacQuarrie, S.; Dasog, M. Highly Efficient, Biochar-Derived Molybdenum Carbide Hydrogen Evolution Electrocatalyst. *Adv. Energy Mater.* **2018**, *8* (29), 1801461. https://doi.org/10.1002/aenm.201801461.

(59) Chen, J.; Gong, M.; Fan, Y.; Feng, J.; Han, L.; Xin, H. L.; Cao, M.; Zhang, Q.; Zhang, D.; Lei, D.; Yin, Y. Collective Plasmon Coupling in Gold Nanoparticle Clusters for Highly Efficient Photothermal Therapy. *ACS Nano.* **2022**, *16* (1), 910–920. https://doi.org/10.1021/acsnano.1c08485.

(60) Fei Guo, C.; Sun, T.; Cao, F.; Liu, Q.; Ren, Z. Metallic Nanostructures for Light Trapping in Energy-Harvesting Devices. *Light Sci. Appl.* **2014**, *3* (4), e161–e161. https://doi.org/10.1038/lsa.2014.42.

(61) Ferraro, A.; Cerza, P.; Mussi, V.; Maiolo, L.; Convertino, A.; Caputo, R. Efficient Photothermal Generation by Nanoscale Light Trapping in a Forest of Silicon Nanowires. *J. P. Chem. C.* **2021**, *125* (25), 14134–14140. https://doi.org/10.1021/acs.jpcc.1c03732.

(62) Wei, X.; Wei, J.; Feng, Y.; Wang, J. Photothermal Hydrophobic Coating with Light-Trapping and Thermal Isolated Effects for Efficient Photothermal Anti-Icing/de-Icing. *Prog. Org. Coat.* **2023**, *179*, 107550. https://doi.org/https://doi.org/10.1016/j.porgcoat.2023.107550.

(63) Wu, L.; Dong, Z.; Cai, Z.; Ganapathy, T.; Fang, N. X.; Li, C.; Yu, C.; Zhang, Y.; Song, Y. Highly Efficient Three-Dimensional Solar Evaporator for High Salinity Desalination by Localized Crystallization. *Nat. Commun.* **2020**, *11* (1), 521. https://doi.org/10.1038/s41467-020-14366-1.

(64) Zhou, X.; Guo, Y.; Zhao, F.; Yu, G. Hydrogels as an Emerging Material Platform for Solar Water Purification. *Acc. Chem. Res.* **2019**, *52* (11), 3244–3253. https://doi.org/10.1021/acs.accounts.9b00455.

(65) Li, X.; Ni, G.; Cooper, T.; Xu, N.; Li, J.; Zhou, L.; Hu, X.; Zhu, B.; Yao, P.; Zhu, J. Measuring Conversion Efficiency of Solar Vapor Generation. *Joule.* **2019**, *3* (8), 1798–1803. https://doi.org/https://doi.org/10.1016/j.joule.2019.06.009.

(66) Zhong, J.; Huang, C.; Wu, D.; Lin, Z. Influence Factors of the Evaporation Rate of a Solar Steam Generation System: A Numerical Study. *Int. J. Heat Mass Transf.* **2019**, *128*, 860–864. https://doi.org/https://doi.org/10.1016/j.ijheatmasstransfer.2018.09.079.

TOC Graphic

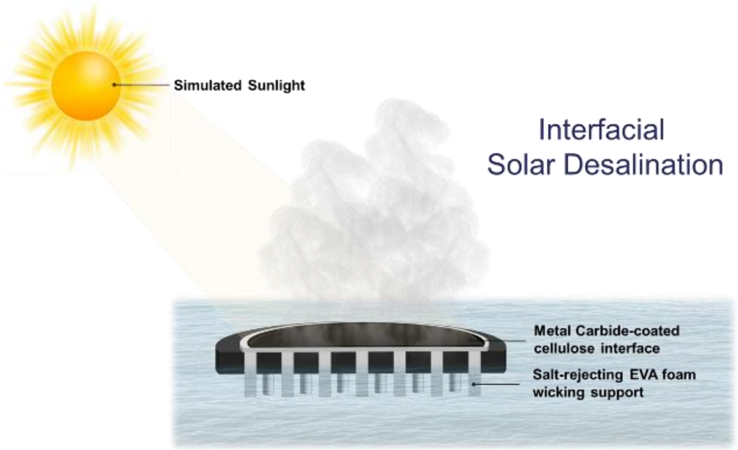
Simulated Sunlight
Interfacial
Solar Desalination
Metal Carbide-coated
cellulose interface
Salt-rejecting EVA foam
wicking support